Exploring Time-Resolved Photoluminescence for Freestanding Nanowires Using a Three-dimensional Computational Transient Model

Dingkun Ren,[*a] Adam C. Scofield,[a] Alan C. Farrell,[a] Zixuan Rong,[a] Michael A. Haddad,[a]

Ramesh B. Laghumavarapu,[a] Baolai Liang[b] and Diana L. Huffaker[a,b,c]

[a]*Department of Electrical and Computer Engineering, University of California at Los Angeles, Los Angeles, California 90095, USA*

[b]*California NanoSystems Institute, University of California at Los Angeles, Los Angeles, California 90095, USA*

[c]*School of Physics and Astronomy, Cardiff University, Cardiff, Wales CF24 3AA, UK*

KEYWORDS

III-V nanowires, TRPL, carrier lifetime, material property, carrier dynamics, GaAs on Si, heterointerfaces

ABSTRACT

Time-resolved photoluminescence (TRPL) has been implemented experimentally to measure the carrier lifetime of III-V semiconductors for decades. For the characterization of freestanding nanowires, the rich information embedded in the TRPL spectra has not been fully interpreted and meaningfully mapped to the respective material properties. This is because their three-dimensional (3-D) geometries result in more complicated mechanisms of carrier recombination than those in thin films and analytical solutions cannot be found for those nanostructures. In this work, we extend the intrinsic capability of TRPL by implementing 3-D computational transient and drift-diffusion simulations to account for the different material properties of a complex structure. We first grow freestanding p-type GaAs nanowires on p-type silicon substrates with GaAs seeds as buffer layers, and we then measure the carrier lifetime and develop a novel simulation approach to fit the TRPL spectra by tuning various material properties in a 3-D transient model. From the resultant TRPL simulations, we identify lifetime characteristics of different material properties considered here, including carrier mobility, Shockley-Read-Hall recombination lifetime, and surface recombination velocity at the GaAs-Si heterointerface. To further interpret the TRPL spectra, we map the spatial and temporal electron distribution across the entire structure and then reveal the underlying carrier dynamics. Based on this technique, we believe TRPL measurement coupled with the 3-D transient model is able to unveil the complex carrier recombination mechanisms in nanostructured materials beyond freestanding nanowires.

Introduction

The bottom-up growth of vertical freestanding nanowires enables heteroepitaxy with large lattice mismatch due to elastic deformation occurred at heterogeneous interfaces.[1, 2] This capability leads to the hybrid integration of III-V nanowire-based electrical and optical devices on silicon/silicon-on-insulator (Si/SOI) platforms, including field-effect transistors,[3-5] lasers,[6-9] light-emitting diodes,[10-18] photodetectors,[19, 20] and solar cells.[21-26] To develop those devices with high performance, it is significant to explore material properties and understand carrier dynamics of freestanding nanowires. However, the characterization of freestanding nanowires is challenging, much more so than that of thin films. This is because the three-dimensional (3-D) geometries of freestanding nanowires have much larger surface-to-volume ratios and smaller cross-sections at the nanowire-substrate heterointerfaces, and therefore analytical solutions cannot be found for such nanostructures.

Over the last decade, remarkable advances in material characterization have taken place, enabling the study of the material properties and carrier dynamics of III-V (or Si) nanowires. As a contactless optical probing technique, time-resolved photoluminescence (TRPL) is commonly used, and it measures the temporal decay of radiative recombination and interprets carrier lifetime that reflects the dynamic process of carriers and the intrinsic recombination mechanisms. For example, lifetime measurement of freestanding GaAs nanowires grown on Si has been attempted to explore trap-induced nonradiative recombination and twinning under various growth conditions and to study surface passivation by introducing an AlGaAs shell.[23, 27-29] Unfortunately, the real-time motion of carriers has not been interpreted, and the interaction of carriers with heterointerfaces and local defects remains unclear. Alternatively, time-resolved THz spectroscopy (also called "optical pump-THz probe") is able to observe relative changes of nanowire trap density and carrier mobility by fitting analytical equations.[30-33] Furthermore, spatially-separated femtosecond pump-probe microscopy is capable of imaging the temporal migration of carriers in individual nanowires with picosecond temporal revolution, which has been implemented to study diameter-dependent carrier lifetime and recombination mechanisms in Si nanowires.[34-37] However, neither spectroscopy

technique is capable of extracting information at the nanowire-substrate interface since nanowires need to be mechanically transferred onto quartz substrates because of either the absorption of in semiconductor substrates in the THz regime or the actual limit of the experimental setup. Since the characterization of freestanding nanowires is more closely related to device performance, the nanowire-substrate interface needs to be included. Additionally, another probing technique called two-photon optical-beam-induced current (TOBIC) has been applied to map 3-D photocurrent current responses for free-standing GaAs photovoltaics grown on GaAs substrates.[38] Still, it has not been adopted to reconstruct the real-time carrier transport or extract multiple material properties.

Although TRPL is traditionally used to measure carrier lifetimes and infer recombination mechanisms, we believe that it has merit and the rich physics underlying TRPL can be harnessed to concurrently explore multiple material properties that reflects complex carrier dynamics for freestanding III-V nanowires as well as those with nanowire-substrate heterointerfaces. This is because the overall lifetime of freestanding nanowires is influenced by the carrier dynamics resulting from not only one but multiple mechanisms. In other words, the lifetime and material properties of a nanowire are related, but not in a simple one-to-one correlation. To prove the concept, we developed a 3-D computational transient model and took a simulation approach to fit the TRPL spectra and carrier lifetimes by tuning various material properties for freestanding GaAs nanowires grown on silicon. Without losing generality, we considered three important material properties, namely, electron mobility (μ_n), Shockley-Read-Hall (SRH) recombination lifetime (τ_{SRH}), and III-V/Si heterointerface recombination velocity (S_n). The first part of this work concerns the growth of high-uniform p-type GaAs nanowires on p-type Si substrates where electrons are the minority carriers. For this, we grew transition layers, i.e., GaAs seeding layers, at different temperatures prior to growing the nanowires. We presumed that those conditions would result in different material properties near the heterointerfaces. Note that we used patterned selective-area epitaxy (SAE) for nanowire growth because the engineered placement of nanowires, e.g., identical periodicity,[39-41] allowed identical optical absorption for each nanowire in the array (except the nanowires close to the edges of array,

where periodicity fails). Then, we measured the minority carrier lifetime (τ_n) and performed TRPL simulation by implementing our 3-D transient model. By tuning the material properties of the GaAs nanowire segment and the GaAs seeding layer, we studied the impact of those properties on τ_n and further identified their lifetime characteristics. Finally, we tabulated the values of material properties based on the simulation results and interpreted the carrier dynamics by mapping spatial electron distribution as a function of time. Again, by using our 3-D computational transient model, we have quantitively studied the impact of each material property on τ_n and the carrier dynamics, and reconstructed real-time carrier transport in those 3-D structures. We believe this work will trigger additional experimental and theoretical work and unveil the real strength of TRPL for exploring carrier dynamics in nanowires and nanostructured materials.

Experimental section

Nanowire growth

The p-type (Zn-doped) GaAs nanowires were grown on lightly boron-doped Si (111) wafers by selective-area metal-organic chemical deposition (SA-MOCVD). A 20nm SiN_x film was deposited as the growth mask. The diameter and pitch of the nanoholes were 80 nm and 800 nm, respectively, defined by electron-beam lithography (EBL). The size of the arrays was designed as 50 μm × 50 μm, much larger than the laser spot size. Since the nanowire growth was sensitive to the cleaning process,[42] we carefully designed the steps to remove the resist. Before the samples were loaded into the growth chamber, native oxide at the Si surface was removed by buffer oxide etch (BOE). Prior to the growth of the nanowire segment, a thin GaAs seeding layer was introduced as a buffer to achieve a high vertical yield and high uniformity across the nanowire array. To generate different GaAs-Si heterointerface material quality, five different growth temperatures for the seeding layers—450°C, 550°C, 600°C, 625°C, and 650°C—were used, while the nanowire growth temperature remained fixed at 730°C. The nanowires were in-situ passivated by a lattice-match AlGaAs shell followed by a thin GaAs to largely reduce the surface recombination at the semiconductor-to-air interfaces. Some published studies of AlGaAs passivation can be found elsewhere.[23, 28, 43] We have labelled

those five samples Sample A (450°C), Sample B (550°C), Sample C (600°C), Sample D (625°C), and Sample E (650°C), respectively. More details of nanowire growth are given in the ESI.†

Nanowire characterization

In order to reconstruct the nanowires in our 3-D transient model, we first investigated the nanowire geometries, i.e., vertical yield, uniformity, and the dimensions of the nanowires as well as the seeding layers. The nanowire dimensions of Samples A through E were measured by scanning electron microscope (SEM). The seeding layer underneath the nanowire segment was characterized by transmission electron microscopy (TEM). Sample C was prepared for TEM analysis by focus ion beam (FIB) milling, and an FEI T12 TEM was operated in bright field to study the GaAs-Si heterointerface region and GaAs nanowire segment. The carrier lifetimes of Samples A to E for band-to-band recombination (875 nm) were carried out by TRPL at room temperature (300 K) using an NKT SuperK EXTREME continuum laser operated at 633 nm with a repetition rate of 40 MHz and a pulse width of 30 ps, an Acton SP-2500i spectrometer (Princeton instruments), a MPD Si single photon avalanche diode (SPAD), and a PicoHarp time-correlated single photon counting module. The laser power intensity was calibrated as 178 W/cm^2 by a power meter (Newport 918D-SL-OD2) and 50× objective lens (Mitutoyo M Plan APO NIR, NA = 0.42). Note that the pumped power of laser is relatively low in order to consider electrons as minority carriers. As shown in the later discussion (in Fig. 6(c) as well), the carrier density of excess electrons is about 1×10^{16} cm^{-3} – 1×10^{17} cm^{-3}; thus, saturation of traps is not likely and all recombination processes should be revealed. In addition, a 695 nm longpass filter was put in front of the spectrometer input slit to block the incident 633 nm laser.

Simulation section

Modeling process

The 3-D computational transient model of the as-grown nanowires was set up by Synopsys® Sentauras TCAD to simulate temporal optical emission from band-to-band radiative recombination, i.e., emission intensity as a function of time, and compare it with experimental optical spectra obtained by TRPL

characterization. The flow of simulation is given as follows. First, we reconstructed a single unit of nanowire arrays including the Si substrate, GaAs seeding layer, and GaAs nanowire segment by using the dimensions measured by SEM and TEM. Then, we computed the optical generation from normally incident picosecond pulse lasers using finite-difference time-domain (FDTD) with period boundary conditions. By combining the Poisson equation, current-density equation, and continuity equation in the transient model, we calculated the temporal band-to-band radiative recombination of both the GaAs nanowire and GaAs seeding layer segments. Finally, τ_n was extracted by an exponential equation with a single decay $exp(-t/\tau)$. Note that Sample A and Sample E are not included in the simulation study since the growth yield is low and the optical absorption is not identical in each nanowire. More explanation will be given later.

Material properties and parameter settings

As mentioned above, three types of material properties are included in the model: electron mobility (μ_n), SRH recombination lifetime (τ_{SRH}), and surface recombination velocity (S_n). Therefore, there are five variables in total: the electron mobility of the nanowire (μ_{n_wire}) and the seeding layer (μ_{n_seed}), the SRH recombination lifetime of the nanowire (τ_{SRH_wire}) and the seeding layer (τ_{SRH_seed}), and surface recombination velocity (S_{n_hetero}) at GaAs-Si heterointerface. Those material properties of Samples B to D will be determined by simulation in the following sections.

To investigate the characteristics of carrier dynamics, we set the values of each material property as follows: (1) electron mobility of nanowire μ_{n_wire} 10 – 500 $cm^2/(V \cdot s)$, (2) electron mobility of seeding layer μ_{n_seed} 0.5 – 10.0 $cm^2/(V \cdot s)$, (3) SRH recombination lifetime of nanowire τ_{SRH_wire} 1.0 ns – 5.0 ns, (4) SRH recombination lifetime of seeding layer τ_{SRH_seed} 0.1 ns – 1.0 ns, and (5) surface recombination velocity at the nanowire-substrate heterointerface S_{n_hetero} 1.0×10^0 cm/s – 1.0×10^6 cm/s. Note that the nonradiative SRH recombination lifetime was considered as a variable, while a constant radiative recombination coefficient of 2.0×10^{-10} cm^3/s was applied to both the nanowire and the seeding layer segments. Additionally, Auger recombination was not significant due to a low level of incident laser power. The hole mobility (μ_p), i.e., the mobility of the majority carrier, was set as 10 times less than the electron mobility (μ_n) (a default

setting). The surface recombination velocity at the nanowire-air interface (S_{n_air}), i.e., at the GaAs/AlGaAs heterointerface, was fixed at 1.0×10^3 cm/s, based on the suggested values in some published studies.[23, 28] All other material parameters were set as default values offered by the material database in the simulator. Importantly, to mimic the TRPL measurement in the simulation, we assumed the temporal profile of the 'laser beam' as a trapezoid—10 ps rise time, 30 ps "on" time, and 10 ps fall time.

Results and discussion

Nanowire growth and carrier lifetimes

The 30°-tilted scanning electron microscope (SEM) images of Samples A through E are shown in Fig. 1(a). Samples B through D show high vertical yield—nearly 100% for Samples B and C and over 85% for Sample D—similar to the growth of un-doped GaAs nanowires by SA-MOCVD.[44] More SEM images of as-grown nanowires are shown in Fig. S2 (ESI†). In contrast, the vertical yield of Samples A and E is much lower, and thus they are not included in the TRPL simulations. The average height and diameter of the vertical nanowires measured by SEM were 740 nm and 135 nm, respectively, as shown in Fig. S3 (ESI†). All five samples showed good uniformity, with a variation of no more than 6 nm. Some irregular polycrystalline structures and tilted nanowire were randomly located inside the arrays. Such random imperfect growth may be due to three factors: (1) the sample cleaning was not sufficient, leaving a small portion of EBL resist around or inside the nanoholes; (2) the surface treatment was not appropriate, giving a mix of Si(111):As 1×1 and Si(111) 1×1; or (3) multiple types of nucleation formed during the seeding layer growth. The third case is most likely, because the formation of seeds by the vapor-solid (VS) growth mode is sensitive to the growth temperature.[45] Therefore, it is fair to expect that the material quality of seeding layers grown at different temperatures will vary.

The cross-section TEM images of Sample C are shown in Fig. 1(b). Crystal defects—zinc-blende (ZB)–wurtzite (WZ) polytypism and stacking faults—were observed, which was expected in patterned SAE growth of III-V nanowires. Thus, the electron mobility of these GaAs nanowires is expected to be much

lower than that of thin-film GaAs or VLS GaAs nanowires due to stronger scattering. Further, no threading dislocations or antiphase domains (APDs) were found in the close-up image of the heterointerface. Interestingly, the seeding layer growth was initiated beneath the SiN_x growth mask, and a trapezoid-shaped GaAs crystalline structure was formed, with a thickness of 6 nm to 7 nm. The formation of such a trapezoidal seeding layer can be explained as follows: During the sample cleaning process, H_2O_2 (in the Piranha solution) and O_2 plasma (in downstream asher) oxidized the top Si surfaces inside the nanoholes, and the oxidized part was removed by BOE. It was expected that the GaAs seeding layer would fill up to the top of the SiN_x mask, as shown in a previous study for InGaAs nanowire growth on Si with GaAs stub (Fig. S6, ref. 9). Thus, the growth beneath the mask was included in the 3-D computational model.

The TRPL spectra of Samples A to E (at 300 K) are shown in Fig. 2, and τ_n of Samples A to E is summarized in the inset. To extract τ_n, the nanowire signals were fitted by a single exponential decay, $exp(-t/\tau)$. The fitting τ_n of band-to-band recombination for Samples A to E are 0.52 ns, 0.84 ns, 1.25 ns, 0.73 ns, and 0.60 ns, respectively. As we expected, τ_n is largely affected by the seeding growth temperature. It is possible that the increase of local defects inside the GaAs seeding layer or at the GaAs-Si heterointerface would lead to the abrupt decrease of τ_n at a lower or higher seeding temperature than 600°C. Compared with the reported studies of intrinsic GaAs nanowires on Si,[27, 46] the Zn-doped GaAs with a 600°C seeding layer (Sample C) shows a comparable minority carrier lifetime. Additionally, it is found that although the growth yield and uniformity of Samples B and C are close, the carrier lifetimes are much different. Thus, we suspect that the quality of GaAs seeding layers have an impact on the material properties of the upper GaAs segments.

3-D transient model with GaAs-Si heterointerfaces

The schematics of an individual unit of as-grown GaAs nanowire on Si substrate is illustrated in Fig. 3(a), where the incident picosecond laser pulses are illuminated from the top. The cross-section of the X-Z plane is shown in Fig. 3(b), and the seeding layer segment and GaAs-Si heterointerface are highlighted in Fig. 3(b), with their dimensions characterized by TEM (Fig. 1(b)). To simplify the simulation structure, we

make several assumptions. First, the nanohole and trapezoid-shaped segments are fully covered by GaAs seed, and their geometries are appoximated as cylindrical, which is similar to the GaAs stubs shown in a previous work (Fig. S6, ref. 9). Second, since the thickness of the AlGaAs passivation layer is estimated as only 5 nm to 10nm, it is not included in the schematics; instead, we describe its property by introducing surface recombination velocity at GaAs/air interfaces on six (110) sidewalls of GaAs nanowires. The energy-band diagram as well as the quasi-Fermi level of the segment along the GaAs-Si heterointerface is shown in Fig. 3(c), and the interface states, i.e., traps, that result in nonradiative recombination are illustrated.

Impacts of material properites on carrier lifetime

To study the impact of material properties on carrier lifetime, we first investigate the contributions from nanowire electron mobility μ_{n_wire} (10 – 500 $cm^2/[V \cdot s]$) as well as surface recombination velocity at the GaAs-Si heterointerface S_{n_hetero} (1.0×10^0 cm/s – 1.0×10^6 cm/s) while τ_{SRH_wire} (5 ns) and τ_{SRH_seed} (1 ns) are constant. Since the GaAs seeding layer was grown at a much lower temperature, it is expected that the material quality of the seed would be much different from that of the nanowire, which is similar to the case for thin-film low-temperature GaAs (LT-GaAs). As a starting point, we assume μ_{n_seed} (1 – 50 $cm^2/[V \cdot s]$) is one tenth of μ_{n_wire} (10 – 500 $cm^2/[V \cdot s]$). Fig. 4(a) shows a contour plot of τ_n as a function of μ_{n_wire} and S_{n_hetero}, which is also marked by three contour lines at 0.84 ns, 1.25 ns, and 0.73 ns, corresponding to the measured τ_n of Samples B through D, respectively. The variation of τ_n due to electron mobilities is remarkable, from 0.029 ns to 2.042 ns with S_{n_hetero} of 1.0×10^0 cm/s and from 0.027 ns to 1.876 ns with S_{n_hetero} of 1.0×10^6 cm/s. Clearly, the change of τ_n exhibits more significant dependency on electron mobility than on surface recombination velocity at the heterointerface. With larger mobility, the diffusion of electrons will be enhanced, which can be intuitively explained by the Eisntein relation $D_n = \mu_n k_B T$, where D_n is the diffucivity of electrons, k_B is the Boltzmann constant, and T is the lattice temperature. In this case, the carriers recombine at the nanowire sidewalls before reaching the GaAs-Si heterointerface, and therefore the nonradiative recombination at the sidewalls will dominate carrier dynamics. Note that the change of τ_n

is almost neligible while S_{n_hetero} is within 1.0×10^{0} cm/s – 1.0×10^{3} cm/s, and it becomes noticeable with higher S_{n_hetero}, suggesting that nonradiative recombination at heterointerfaces surpasses the recombination at other surfaces. In short, if only S_{n_hetero} is varied, τ_n cannot vary from 0.73 ns to 1.25 ns, and therefore other material properties must be concurrently changed as well while the seeding layer growth temperature is altered. Fig. 4(b) illustrates the simulated TRPL spectra, i.e., radiative recombination of GaAs as a function of time, with a constant S_{n_hetero} of 1.0×10^{0} cm/s and a series of μ_{n_wire} from 10 $cm^2/(V\cdot s)$ to 75 $cm^2/(V\cdot s)$. The intensity of emission is maximized at 60 ps and starts to decay with carrier diffusion and recombination. The overall τ_n is changed from 2.04 ns to 0.55 ns, which again shows a large impact of electron mobility on carrier recombination.

So far, we fix τ_{SRH_wire} at 5 ns and τ_{SRH_seed} at 1 ns, which would presumably be high for GaAs nanowires grown on Si substrates. Interestingly, we find that τ_n can be as low as tens of ps with high carrier mobility and significant carrier diffusion. Therefore, observing a short nanowire lifetime experiment does not necessarily mean that the actual lifetime is short or other material properties are imperfect—the impact of mobility must be considered. Based on the results given in Fig. 4, it would be fair to assume that the simulated τ_n with S_{n_hetero} of 1.0×10^{0} cm/s sets the upper limit, and the actual τ_n would be shorter due to smaller values of actual τ_{SRH_wire} and τ_{SRH_seed}. Since μ_{n_wire} yields a mobility of 10~75 $cm^2/(V\cdot s)$ (more likely toward 10 $cm^2/(V\cdot s)$), we fix the value at 25 $cm^2/(V\cdot s)$ for the next step of the simulation.

Next, we vary four other material properties: τ_{SRH_wire} (1 ns – 5 ns), τ_{SRH_seed} (0.1 – 1.0 ns), S_{n_hetero} (1.0×10^{0} cm/s – 1.0×10^{6} cm/s), and μ_{n_seed} (0.5 – 10 $cm^2/[V\cdot s]$). Fig. 5(a) shows four 3-D contour plots of τ as a function of τ_{SRH_wire}, τ_{SRH_seed}, and S_{n_hetero} with a constant μ_{n_seed} of 0.5 $cm^2/(V\cdot s)$, 1.0 $cm^2/(V\cdot s)$, 5.0 $cm^2/(V\cdot s)$, and 10.0 $cm^2/(V\cdot s)$, respectively. As in the previous case, increasing μ_{n_seed} results in decreasing τ_n, suggesting that the carriers would diffuse faster to the interfaces and then recombine. As for SRH recombination, τ_{SRH_wire} shows a larger impact on τ than τ_{SRH_seed}, which is because the nanowire segment carries more minority carriers due to having a larger spatial volume than the seeding layer. As for S_{n_hetero}, it barely affects τ while it is smaller than 1.0×10^{4} cm/s and then becomes more dominant when it becomes larger than 1.0×10^{4} cm/s.

To further investigate the correlation between τ_n and material properties, we resummarize the lifetime information from each coutour plot in Fig. 5(a) and replot it in box charts, as shown in Fig. 5(b). Each box (shown in green) in Fig. 5(b) presents a range of τ_n while altering τ_{SRH_seed} (1 ns – 5 ns) and S_{n_hetero} (1.0×10^0 cm/s – 1.0×10^6 cm/s) and keeping τ_{SRH_wire} and μ_{n_seed} constant. In other words, the box offers estimated values of τ_n for different growth conditions of the GaAs seeding layer and the GaAs-Si heterointerface. In addition, each box chart is labeled with three dashed lines, showing the boundaries of measured τ_n, i.e., 1.25 ns, 0.84 ns, and 0.73 ns. Clearly, τ_n is more sensitive to the material qualities of the GaAs seeding layer with smaller μ_{n_seed}. In addition, with longer τ_{SRH_wire}, it would be more likely that electrons in the nanowire could diffuse into the seeding layer. Therefore, the overall τ_n exhibits more dependency on material properties of the seeding layer. Note that no single box in those four charts is able to cover a full range of τ_n from 0.73 ns to 1.25 ns, meaning that τ_n cannot be varied from 0.73 ns to 1.25 ns by changing only τ_{SRH_seed} or S_{n_hetero}. In other words, the observed range of lifetimes for Samples B to D cannot be explained purely by a difference in GaAs-Si heterointerface quality. Again, it is highly possible that the GaAs seeding layer is affecting the upper GaAs segment—the material quality of the nanowire is concurrently degraded while the growth temperature of the seeding layer is lower or higher than 600°C. Though the growth conditions of nanowire segments for all samples are consistent, local defects might be introduced at the seed-nanowire interface and then affect the growth quality of nanowire segments.

Equipped with some insights into those correlations, we now perform an analysis to estimate possible values of τ_{SRH_wire}, τ_{SRH_seed}, S_{n_hetero} and μ_{n_seed}. As shown in Fig. 5(b), with μ_{n_seed} = 10.0 cm^2/(V·s), τ_n cannot be over 1.25 ns, indicating that the actual mobililty of all those samples would be lower. To cover τ_n from 0.73 ns to 1.25 ns, the ranges of τ_{SRH_wire} would be 1.2 ns to 2.3 ns, 1.4 to 2.5 ns, and 1.4 to 4.0 ns for μ_{n_seed} = 0.5 cm^2/(V·s), 1.0 cm^2/(V·s), and 5.0 cm^2/(V·s), respectively. We expect that the material quality of both the nanowire and seed segments for Sample C is the best among all samples. Thus, it is preferred that the line of 1.25 ns crosses the top portion of the box where τ_{SRH_seed} is high and S_{n_hetero} is low, while the bottom boundary of 0.73 ns intersects the bottom part of the box. It is more likely that μ_{n_seed} is less than 5.0 cm^2/(V·s), because we expect that the change of τ_{SRH_wire} resulting from the seeding layer

growth temperature would not be significant and around 1 ns or so. A more complete spreadsheet that list the simulated τ_n as a function of material properties is given in the ESI.† Based on those simualtion results, we suggested the value for each material property, as listed in Table 1. As expected, the lifetime and material properties of a free-standing nanowire are certainly intercorrelated instead of in a simple one-to-one correlation.

Carrier dynamics

After determining the fitting parameters for Samples B through D, we move on to probe the real-time carrier dynamics of electrons. The temporal and spatial information of electron distribution provides further insight into carrier motion and the recombination mechnism for our 3-D structure. Fig. 6(a) illustrates the simulated TRPL spectra to fit measurements (shown in Fig. 2) by using suggested values for each material property listed in Table 1. Fig. 6(b) shows the finite-difference time-domain (FDTD) simulation of optical generation of the entire structure and its cross-section (Y-Y plane) under incident light at 633 nm. Compared with GaAs segments, the optical absorption in the Si substrate is much less due to its smaller absorption coefficient. Note that the photogenerated carriers are mostly concentrated in the top and bottom regions of the nanowire as well as the area near the GaAs-Si heterointerface. Clearly, those generated carriers close to the seeding layer are more likely to diffuse to the heterointerface than the carriers around the nanowire tip. The simulated spatial distributions of electrons at different points of time, i.e., 30 ps, 60 ps, 100 ps, 300 ps, 600 ps, and 1000 ps, for Samples B through D are illustrated in Fig. 6(c). At the intial stage, the density of photogenerated minority carriers keeps increasing when the samples are exposed under laser pulses from 10 ps to 60 ps. Then, from 60 ps to 1000 ps, electrons in the nanowire segment start to diffuse either toward the top or downward to the GaAs-Si heterointerface, while the density of electrons decreases due to the SRH recombination in the nanowires or at the sidewall. Similarly, electrons in the Si substrate diffuse toward Si/SiN_x and GaAs-Si and recombine. It is obvious that, starting from 100 ps, the electron density inside the nanowire of Sample C is larger than that of Samples B and D, which is due to a larger τ_{SRH}. We also note that the electron density close to the GaAs-Si heterointerface decreases with increasing S_n from

Sample C to Samples B and D. Due to the intrinsic large surface-to-volume ratio for nanowires, τ_n would be largely affected by aspects of the nanowire itself rather than the nanowire-subtrate heterointerface, unless the recombination in the GaAs seeding layer and at the heterointerface is extremely significant, which would surpass the recombination along the nanowire sidewalls. Another possible approach to make recombination at the GaAs-Si heterointerface dominant is to properly design the patterns of nanowire array or nanowire dimensions, which would result in optical generation mostly close to the heterointerfaces.

Conclusions

In summary, we explored the feasibility of revealing multiple material properties by TRPL measurement combined with simulation for freestanding nanowires with nanowire-substrate heterointerfaces. Those material properties included electron mobility, SRH recombination lifetime, and surface recombination velocity at heterointerfaces. The strategy was to reproduce experimental TRPL spectra by a 3-D transient model with reasonable fitting parameters for the material properties considered here. To prove the concept, we grew p-type GaAs nanowires on p-type Si by SA-MOCVD and measured minority carrier lifetime. Prior to nanowire growth, a GaAs seeding layer was introduced at a lower temperature to increase the growth uniformity. Using our transient model, we found that the seeding layers grown at different temperatures would result in different material properties for nanowires, seeding layers, and GaAs-Si heterointerfaces. In order to obtain more information by TRPL, it is necessary to include more material properties in the simulation to form a comprehensive 3-D model. We believe the presented experimental and theoretical studies will stimulate validating work and unveil the hidden power of TRPL for fundamental research on nanowires and nanostructured materials.

†Electronic Supplementary Information (ESI)

Additional information related to the experiments and simulations.

Corresponding Author

*Email: dingkun.ren@ucla.edu

Funding sources

The Air Force Office of Scientific Research (grant no. FA-9550-12-1-0052), the National Science Foundation (grant no. ECCS-1314253), the UC Laboratory Fees Research Program (grant no. 12-LR-238568), the United Sates Department of Defense (grant no. NSSEFF N00244-09-1-0091), and Sêr Cymru National Research Network in Advanced Engineering and Materials.

Competing financial interests

There are no conflicts of interest to declare.

Acknowledgements

We would like to acknowledge the user facilities – UCLA Nanoelectronics Research Facility as well as Integrated Systems Nanofabrication Cleanroom (ISNC) and Electron Imaging Center for NanoMachines (EICN) in California NanoSystems Institute (CNSI). We also gratefully acknowledge the support from the Air Force Office of Scientific Research (grant no. FA-9550-12-1-0052), the National Science Foundation (grant no. ECCS-1314253), the UC Laboratory Fees Research Program (grant no. 12-LR-238568), and the United Sates Department of Defense (grant no. NSSEFF N00244-09-1-0091). In addition, the authors would like to acknowledge the financial support provided by Sêr Cymru National Research Network in Advanced Engineering and Materials.

References

1. K. A. Dick and P. Caroff, *Nanoscale*, 2014, **6**, 3006-3021.
2. D. Ren, A. C. Farrell, B. S. Williams and D. L. Huffaker, *Nanoscale*, 2017, **9**, 8220-8228.
3. K. Tomioka and T. Fukui, *Applied Physics Letters*, 2011, **98**, 083114.
4. K. Tomioka, M. Yoshimura and T. Fukui, *Nature*, 2012, **488**, 189-192.
5. K. Tomioka, M. Yoshimura and T. Fukui, *Nano Letters*, 2013, **13**, 5822-5826.
6. B. Mayer, L. Janker, B. Loitsch, J. Treu, T. Kostenbader, S. Lichtmannecker, T. Reichert, S. Morkötter, M. Kaniber, G. Abstreiter, C. Gies, G. Koblmüller and J. J. Finley, *Nano Letters*, 2016, **16**, 152-156.
7. H. Kim, W.-J. Lee, A. C. Farrell, J. S. D. Morales, P. Senanayake, S. V. Prikhodko, T. J. Ochalski and D. L. Huffaker, *Nano Letters*, 2017, **17**, 3465-3470.
8. K. H. Li, LiuX, WangQ, ZhaoS and MiZ, *Nat Nano*, 2015, **10**, 140-144.
9. R. Chen, T.-T. D. Tran, K. W. Ng, W. S. Ko, L. C. Chuang, F. G. Sedgwick and C. Chang-Hasnain, *Nat Photon*, 2011, **5**, 170-175.
10. C. P. T. Svensson, M. Thomas, T. Johanna, L. Christina, R. Michael, H. Dan, S. Lars and O. Jonas, *Nanotechnology*, 2008, **19**, 305201.
11. K. Tomioka, J. Motohisa, S. Hara, K. Hiruma and T. Fukui, *Nano Letters*, 2010, **10**, 1639-1644.
12. W. Guo, M. Zhang, A. Banerjee and P. Bhattacharya, *Nano Letters*, 2010, **10**, 3355-3359.
13. N. Hieu Pham Trung, C. Kai, Z. Shaofei, F. Saeed and M. Zetian, *Nanotechnology*, 2011, **22**, 445202.
14. W. Guo, A. Banerjee, P. Bhattacharya and B. S. Ooi, *Applied Physics Letters*, 2011, **98**, 193102.
15. K. Tomioka, T. Tanaka, S. Hara, K. Hiruma and T. Fukui, *IEEE Journal of Selected Topics in Quantum Electronics*, 2011, **17**, 1112-1129.
16. N. Hieu Pham Trung, D. Mehrdad, C. Kai and M. Zetian, *Nanotechnology*, 2012, **23**, 194012.
17. M.-H. Bae, B.-K. Kim, D.-H. Ha, S. J. Lee, R. Sharma, K. J. Choi, J.-J. Kim, W. J. Choi and J. C. Shin, *Crystal Growth & Design*, 2014, **14**, 1510-1515.
18. E. Dimakis, U. Jahn, M. Ramsteiner, A. Tahraoui, J. Grandal, X. Kong, O. Marquardt, A. Trampert, H. Riechert and L. Geelhaar, *Nano Letters*, 2014, **14**, 2604-2609.
19. A. Brenneis, J. Overbeck, J. Treu, S. Hertenberger, S. Morkötter, M. Döblinger, J. J. Finley, G. Abstreiter, G. Koblmüller and A. W. Holleitner, *ACS Nano*, 2015, **9**, 9849-9858.
20. M. D. Thompson, A. Alhodaib, A. P. Craig, A. Robson, A. Aziz, A. Krier, J. Svensson, L.-E. Wernersson, A. M. Sanchez and A. R. J. Marshall, *Nano Letters*, 2016, **16**, 182-187.
21. J. C. Shin, K. H. Kim, K. J. Yu, H. Hu, L. Yin, C.-Z. Ning, J. A. Rogers, J.-M. Zuo and X. Li, *Nano Letters*, 2011, **11**, 4831-4838.
22. J. C. Shin, P. K. Mohseni, K. J. Yu, S. Tomasulo, K. H. Montgomery, M. L. Lee, J. A. Rogers and X. Li, *ACS Nano*, 2012, **6**, 11074-11079.

23. N. Jiang, P. Parkinson, Q. Gao, S. Breuer, H. H. Tan, J. Wong-Leung and C. Jagadish, *Applied Physics Letters*, 2012, **101**, 023111.

24. J. C. Shin, A. Lee, P. Katal Mohseni, D. Y. Kim, L. Yu, J. H. Kim, H. J. Kim, W. J. Choi, D. Wasserman, K. J. Choi and X. Li, *ACS Nano*, 2013, **7**, 5463-5471.

25. J. Wu, Y. Li, J. Kubota, K. Domen, M. Aagesen, T. Ward, A. Sanchez, R. Beanland, Y. Zhang, M. Tang, S. Hatch, A. Seeds and H. Liu, *Nano Letters*, 2014, **14**, 2013-2018.

26. M. Yao, S. Cong, S. Arab, N. Huang, M. L. Povinelli, S. B. Cronin, P. D. Dapkus and C. Zhou, *Nano Letters*, 2015, **15**, 7217-7224.

27. J. H. Kang, Q. Gao, P. Parkinson, H. J. Joyce, H. H. Tan, Y. Kim, Y. Guo, H. Xu, J. Zou and C. Jagadish, *Nanotechnology*, 2012, **23**, 415702.

28. N. Jiang, Q. Gao, P. Parkinson, J. Wong-Leung, S. Mokkapati, S. Breuer, H. H. Tan, C. L. Zheng, J. Etheridge and C. Jagadish, *Nano Letters*, 2013, **13**, 5135-5140.

29. F. Wang, Q. Gao, K. Peng, Z. Li, Z. Li, Y. Guo, L. Fu, L. M. Smith, H. H. Tan and C. Jagadish, *Nano Letters*, 2015, **15**, 3017-3023.

30. P. Parkinson, H. J. Joyce, Q. Gao, H. H. Tan, X. Zhang, J. Zou, C. Jagadish, L. M. Herz and M. B. Johnston, *Nano Letters*, 2009, **9**, 3349-3353.

31. P. Parkinson, C. Dodson, H. J. Joyce, K. A. Bertness, N. A. Sanford, L. M. Herz and M. B. Johnston, *Nano Letters*, 2012, **12**, 4600-4604.

32. H. J. Joyce, P. Parkinson, N. Jiang, C. J. Docherty, Q. Gao, H. H. Tan, C. Jagadish, L. M. Herz and M. B. Johnston, *Nano Letters*, 2014, **14**, 5989-5994.

33. J. L. Boland, S. Conesa-Boj, P. Parkinson, G. Tütüncüoglu, F. Matteini, D. Rüffer, A. Casadei, F. Amaduzzi, F. Jabeen, C. L. Davies, H. J. Joyce, L. M. Herz, A. Fontcuberta i Morral and M. B. Johnston, *Nano Letters*, 2015, **15**, 1336-1342.

34. M. M. Gabriel, J. R. Kirschbrown, J. D. Christesen, C. W. Pinion, D. F. Zigler, E. M. Grumstrup, B. P. Mehl, E. E. M. Cating, J. F. Cahoon and J. M. Papanikolas, *Nano Letters*, 2013, **13**, 1336-1340.

35. E. M. Grumstrup, M. M. Gabriel, E. E. M. Cating, E. M. Van Goethem and J. M. Papanikolas, *Chemical Physics*, 2015, **458**, 30-40.

36. E. M. Grumstrup, M. M. Gabriel, E. M. Cating, C. W. Pinion, J. D. Christesen, J. R. Kirschbrown, E. L. Vallorz, J. F. Cahoon and J. M. Papanikolas, *The Journal of Physical Chemistry C*, 2014, **118**, 8634-8640.

37. E. M. Grumstrup, M. M. Gabriel, C. W. Pinion, J. K. Parker, J. F. Cahoon and J. M. Papanikolas, *Nano Letters*, 2014, **14**, 6287-6292.

38. P. Parkinson, Y.-H. Lee, L. Fu, S. Breuer, H. H. Tan and C. Jagadish, *Nano Letters*, 2013, **13**, 1405-1409.

39. A. C. Scofield, J. N. Shapiro, A. Lin, A. D. Williams, P.-S. Wong, B. L. Liang and D. L. Huffaker, *Nano Letters*, 2011, **11**, 2242-2246.

40. P. Senanayake, C.-H. Hung, J. Shapiro, A. Lin, B. Liang, B. S. Williams and D. L. Huffaker, *Nano Letters*, 2011, **11**, 5279-5283.

41. G. Mariani, A. C. Scofield, C.-H. Hung and D. L. Huffaker, *Nat Communications*, 2013, **4**, 1497.

42. J. G. Sandra, P. B. Jonathan and R. L. Ray, *Semiconductor Science and Technology*, 2013, **28**, 105025.

43. K. Komolibus, A. C. Scofield, K. Gradkowski, T. J. Ochalski, H. Kim, D. L. Huffaker and G. Huyet, *Applied Physics Letters*, 2016, **108**, 061104.

44. T. Katsuhiro, K. Yasunori, M. Junichi, H. Shinjiroh and F. Takashi, *Nanotechnology*, 2009, **20**, 145302.

45. E. Russo-Averchi, M. Heiss, L. Michelet, P. Krogstrup, J. Nygard, C. Magen, J. R. Morante, E. Uccelli, J. Arbiol and A. Fontcuberta i Morral, *Nanoscale*, 2012, **4**, 1486-1490.

46. A. M. Munshi, D. L. Dheeraj, V. T. Fauske, D. C. Kim, J. Huh, J. F. Reinertsen, L. Ahtapodov, K. D. Lee, B. Heidari, A. T. J. van Helvoort, B. O. Fimland and H. Weman, *Nano Letters*, 2014, **14**, 960-966.

For Table of Contents Only

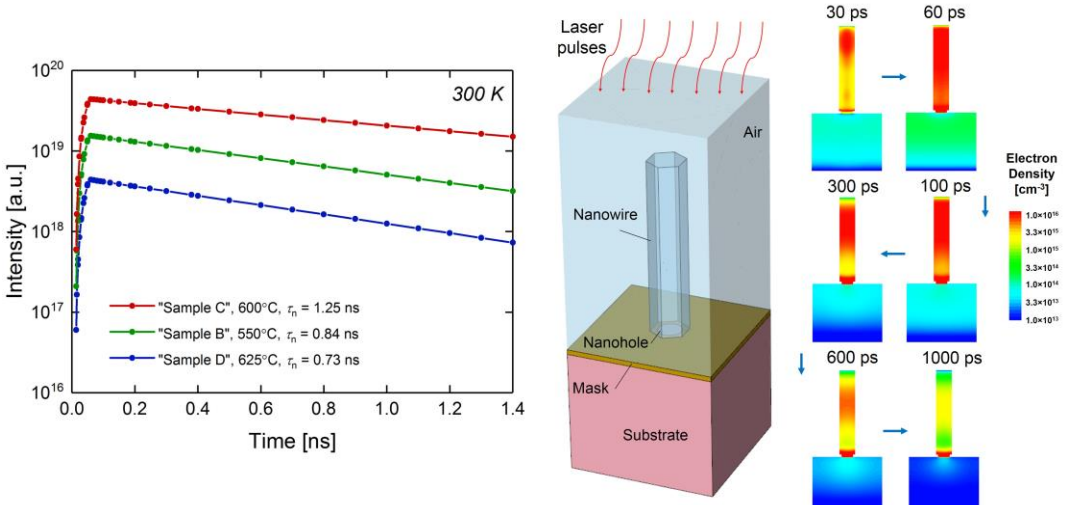

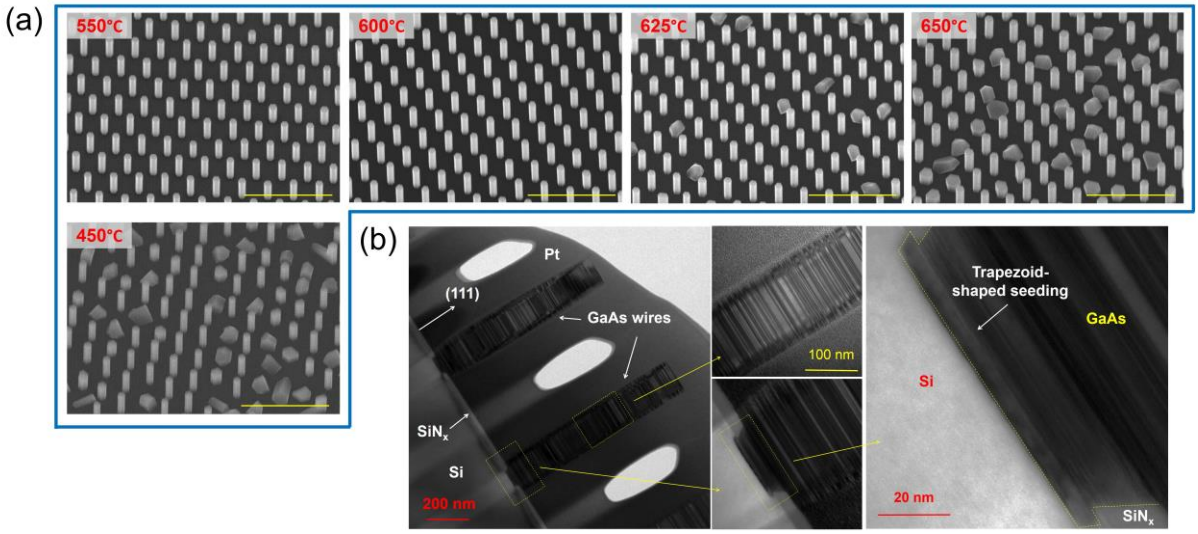

Fig. 1 *(a) 30°-tilted SEM of as-grown GaAs nanowires on Si substrates with AlGaAs passivation layers. The seeding layers were grown at 450°C, 550°C, 600°C, 620°C and 650°C, respectively. The scale bar is 2 µm. (b) Cross-sectional TEM image of GaAs nanowires with GaAs seeding layer grown at 600 °C. The two zoom-in images in the center show the nanowire segment and the trapezoid-shaped seeding layer. The further close-up detail of GaAs-Si interface is shown in the image on the right.*

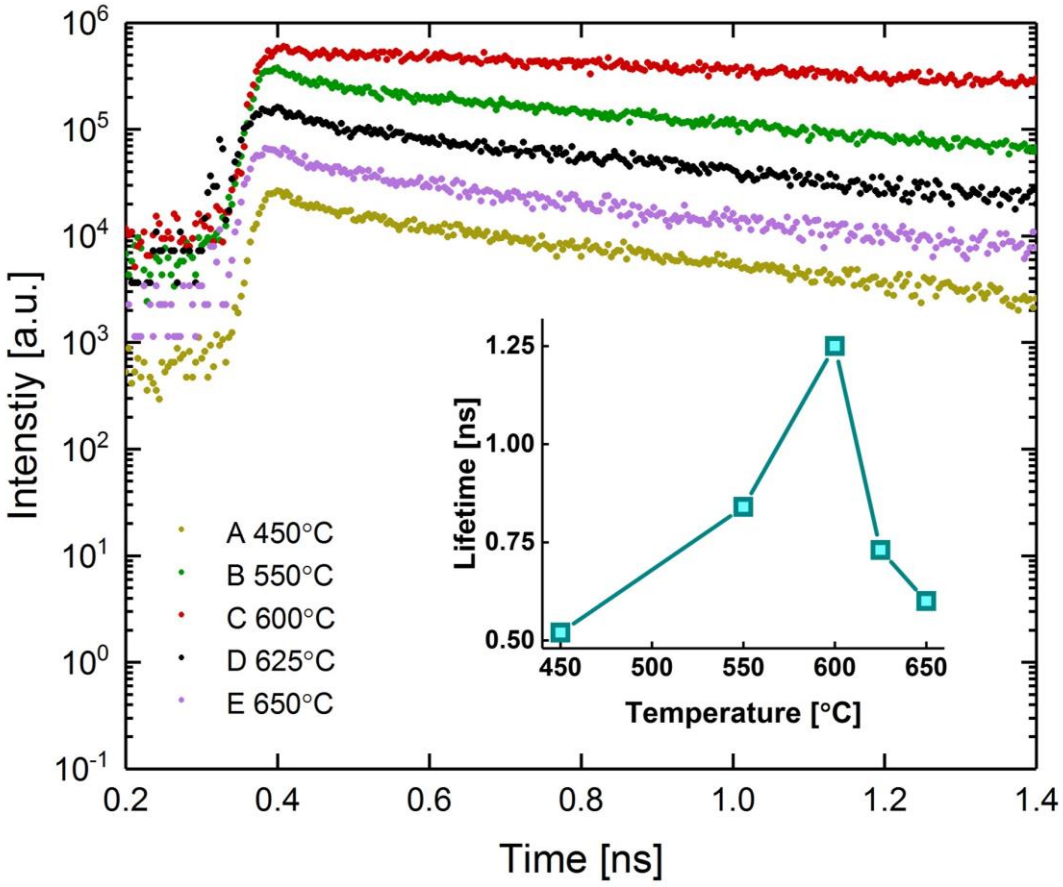

Fig. 2 *The TRPL spectra of Samples A to E at 300 K. The seeding layer growth temperatures of those three samples are 450°C, 550°C, 600°C, 620°C and 650°C, respectively. In the inset, the extracted lifetimes of Samples A to E are all given.*

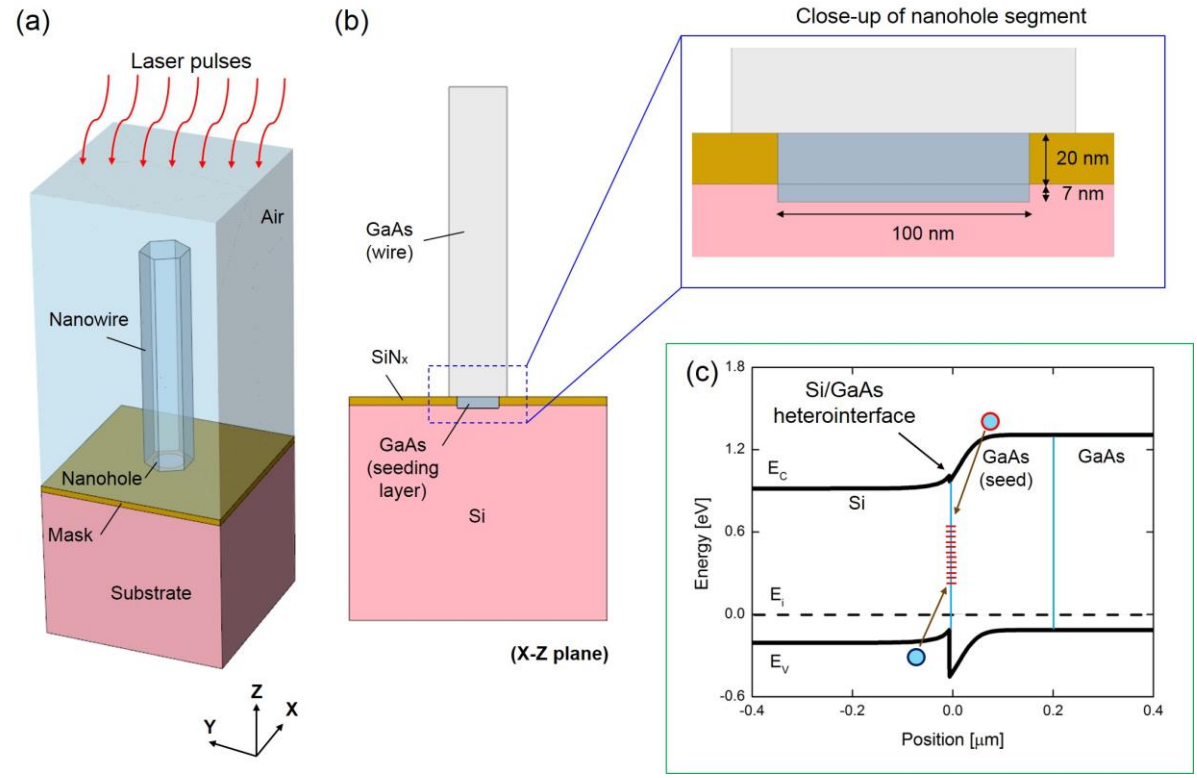

Fig. 3 *3-D modeling of selective-area GaAs nanowires on Si for minority carrier lifetime simulation. (a) Schematics of 3-D model for FDTD simulation and FEM electrical simulation. (b) The cross-section of 3-D model showing the close-up of GaAs seeding layer. Its dimensions are measured by cross-sectional TEM. (c) Energy-band diagram of p-type GaAs-Si heterointerface. The interface states are illustrated.*

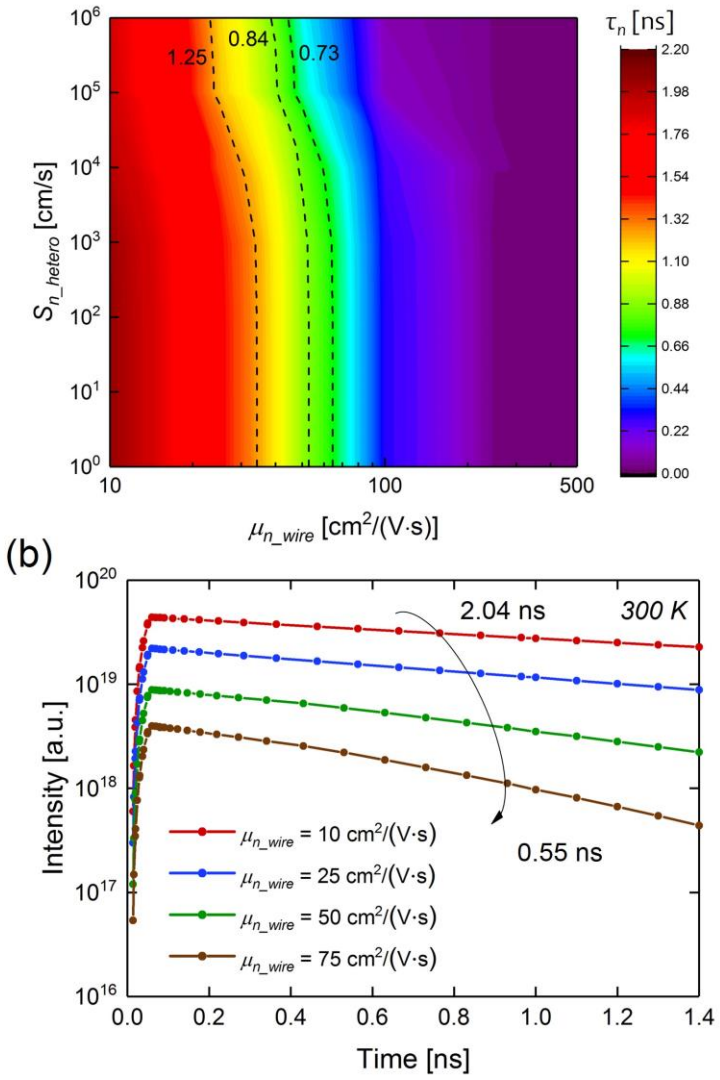

Fig. 4 *Determining electron mobility of GaAs nanowire μ_{n_wire}. (a) Contour plot of simulated minority carrier lifetime τ_n as a function of μ_{n_wire} (10 – 500 cm^2/[V·s]) and S_{n_hetero} (10^0 – 10^6 cm/s). selective-area GaAs nanowires on Si for minority carrier lifetime simulation. Three contour lines correspond to the measured lifetime of Samples B to D: 0.73 ns, 1.25 ns, and 0.84 ns, respectively. (b) Simulated TRPL spectra at room temperature with different μ_{wire} of 10 cm^2/(V·s), 25 cm^2/(V·s), 50 cm^2/(V·s), and 75 cm^2/(V·s), which correspond to τ_n* of 2.04 ns, 1.47 ns, 0.89 ns, and 0.55 ns, respectively. *The values of other material properties used in the simulation are given: μ_{n_seed} = 0.1× μ_{n_wire}, τ_{SRH_wire} = 5 ns, and τ_{SRH_wire} = 1 ns.*

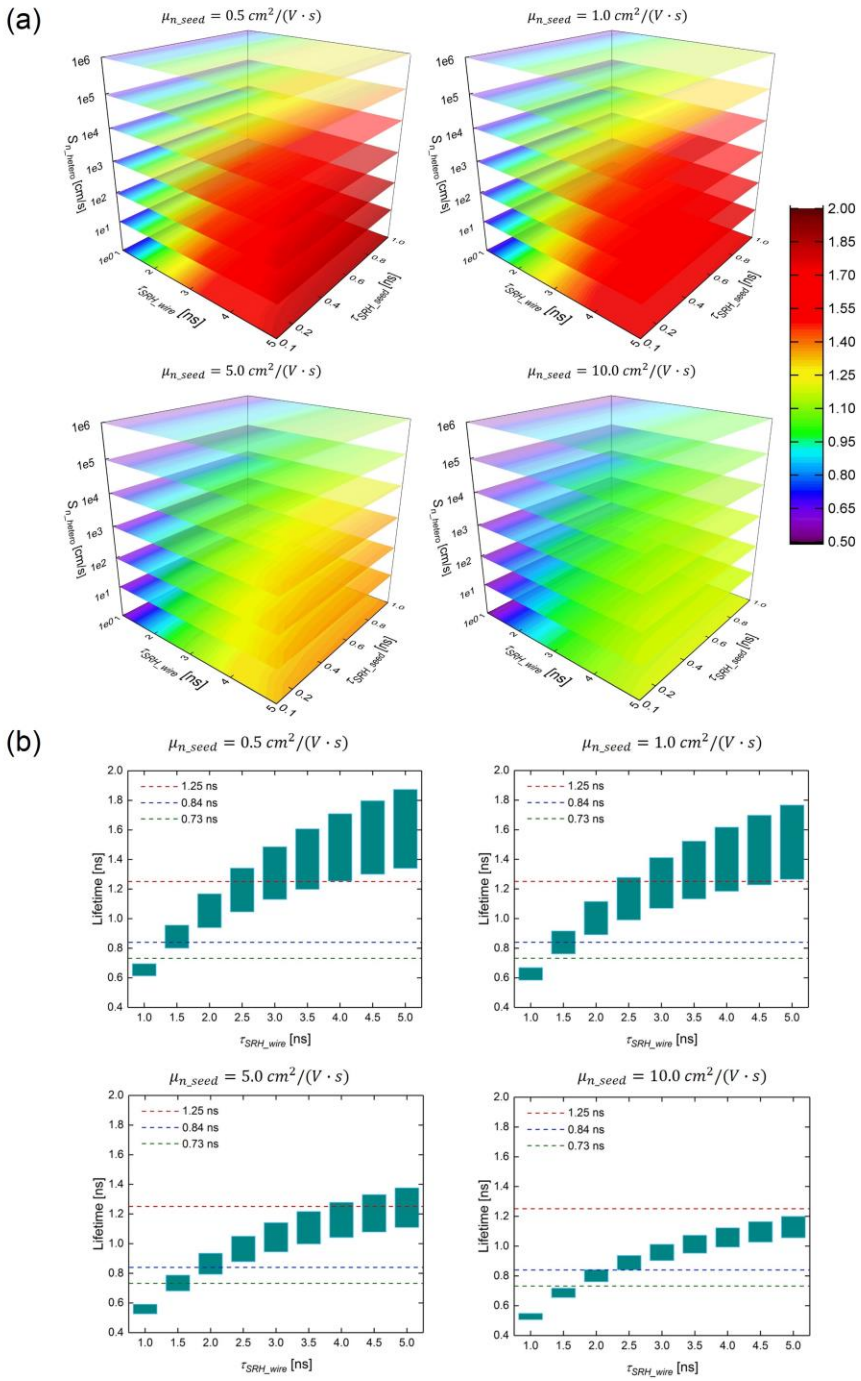

Fig. 5 *The relation of minority carrier lifetime τ_n with other four material properties μ_{n_seed}, τ_{SRH_wire}, τ_{SRH_seed}, and S_{n_hetero}. (a) 3-D contour plots of simulated τ_n as a function of τ_{SRH_wire} (1 – 5 ns), τ_{SRH_seed} (0.1 – 1 ns), and S_{n_hetero} (10^0 – 10^6 cm/s). The electron mobility of seeding layer μ_{n_seed} (0.5 – 10.0 $cm^2/[V{\cdot}s]$) is fixed for each plot. (b) Box charts summarizing all possible values of τ_n as a function of τ_{SRH_wire} based on (a). Each box shows a range of τ_n by varying seeding layer properties τ_{SRH_seed} (0.1 – 1 ns) and S_{n_hetero} (10^0 – 10^6 cm/s).*

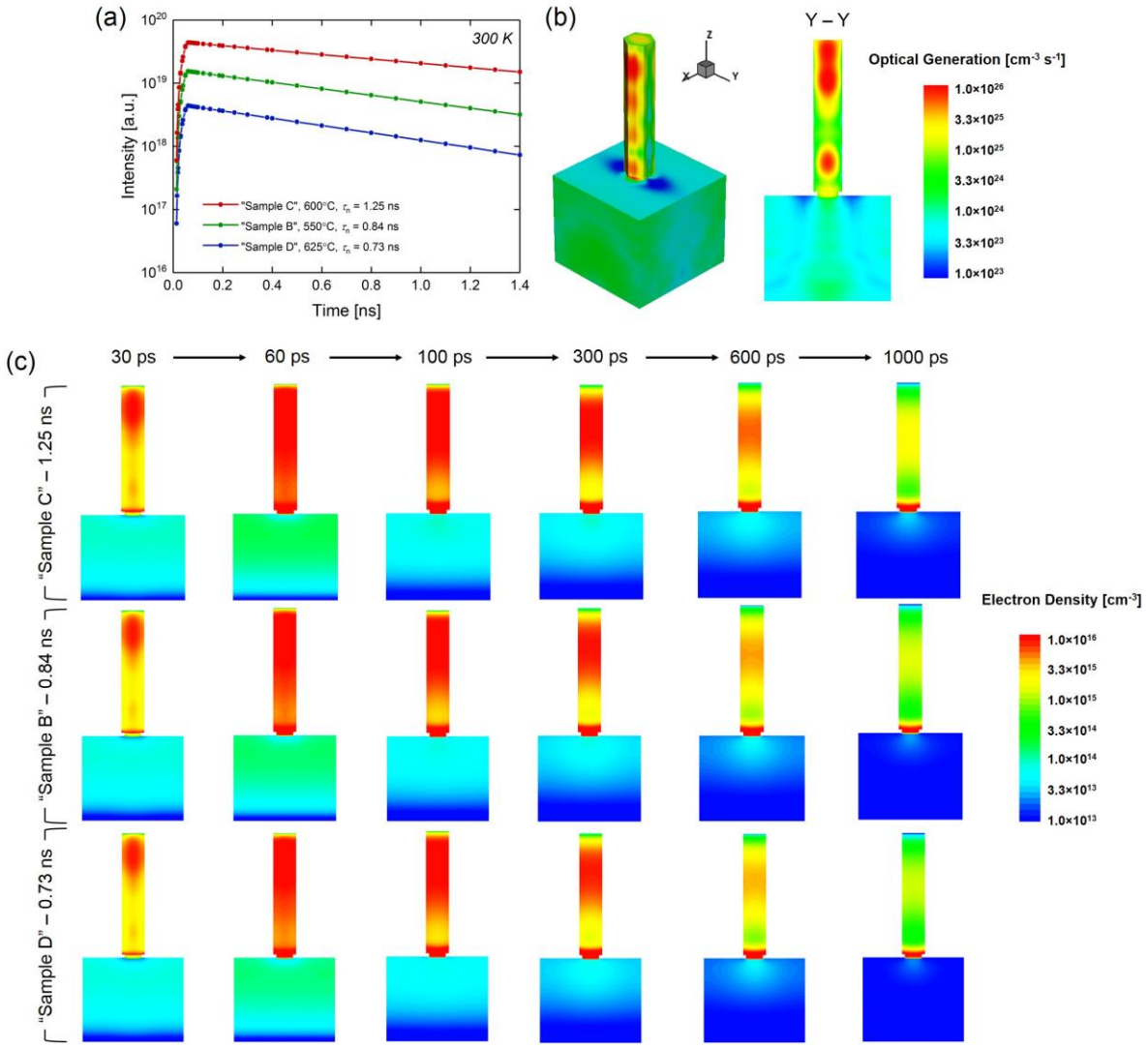

Fig. 6 *Fitting TRPL spectra of Samples B – D and unveiling carrier dynamics. (a) Simulated TRPL spectra at room temperature with fitting values listed in Table 1. (b) FDTD simulation showing optical generation under top illumination at 633 nm with an incident power of 178 W/cm^2. (c) Simulated spatial distribution of electrons at different points of time – 30 ps, 60 ps, 100 ps, 300 ps, 600 ps, and 1000 ps, respectively.*

Table 1 Suggested values of material properties for Sample B, Sample C, and Sample D

Sample	T_{Seed} [°C]	τ_n [ns]	μ_{n_wire} [$cm^2/(V \cdot s)$]	μ_{n_seed} [$cm^2/(V \cdot s)$]	τ_{SRH_wire} [ns]	τ_{SRH_seed} [ns]	S_n [cm/s]
B	550	0.73	25	1	1.5	0.2	1×10^5
C	600	1.25	25	1	2.5	0.3	1×10^2
D	625	0.84	25	1	1.4	0.1	1×10^4